Rheologic contraints on the Lithosphere and Asthenosphere from five years of Postseismic deformation following the El Mayor-Cucapah earthquake

T. T. Hines[1], E. A. Hetland[1]

Abstract

foo bar

1. Introduction

Ground deformation in the years following a large (>Mw7) earthquake provides insight into the mechanical behaviour of the lithosphere. It has long been recognized that interpretations of postseismic deformation can be ambiguous because multiple postseismic deformation mechanisms can have qualitatively similar surface expressions (e.g. [39]). Thanks to the dense geodetic network deployed throughout the 2000's as part of the Plate Boundary Observatory, the April 4, 2010, Mw7.2 El Mayor-Cucapah earthquake in Baja California produced observable postseismic deformation at more GPS stations than any other earthquake in California to date. With such a large collection of data, we attempt to discern the mechanisms driving postseismic deformation following the El Mayor-Cucapah earthquake, where we consider both afterslip and viscoelastic relaxation in lithosphere and asthenosphere as candidate mechanisms.

Previous studies which have modeled postseismic deformation following the El Mayor-Cucapah earthquake include Pollitz et al. [34], Gonzalez-Ortega et al. [11], Spinler et al. [43], and Rollins et al. [38]. Of these studies, Gonzalez-Ortega et al. [11] and Rollins et al. [38] have attempted to describe the observations with afterslip in an entirely elastic lithosphere and asthenosphere. Gonzalez-Ortega et al. [11] described five months of postseismic deformation observed by nearfield ($\lesssim$ 50 km from the rupture) campaign GPS and InSAR with afterslip and contraction on the coseismically ruptured fault. Gonzalez-Ortega et al. [11] noted that their preferred model underestimated the GPS displacements for stations $\gtrsim$ 25 km from the rupture and suggested that it could be the result of unmodeled viscoelastic relaxation. Using continuous GPS stations, which are mostly north of rupture zone, Rollins et al. [38] found that three years of postseismic deformation can be adequately explained by afterslip, albeit with an implausibly large amount of afterslip inferred on the least constrained, southern most fault segment. Here, we suggest this inferred afterslip may have been acting as a proxy for distributed relaxation in the upper mantle.

[1]Department of Earth and Environmental Sciences, University of Michigan, Ann Arbor, MI, USA

Pollitz et al. [34], Rollins et al. [38] and Spinler et al. [43] have explored viscoelastic relaxation in the lower crust and upper mantle as a potential postseismic deformation mechanism. The lithospheric rheology is largely unknown and so modeling postseismic deformation with viscoelastic relaxation requires one to assume a rheologic model and then find the best fitting rheologic parameters. The inference of these rheologic parameters is a computationally expensive nonlinear inverse problem which is typically approached with a forward modeling grid search method. Consequently, a simplified structure for the lithosphere must be made to minimize the number of rheologic parameters that need to be estimated. For example, it is commonly assumed that the lithosphere consists of only three homogeneous, Maxwell viscoelastic layers, which may be an inadequate representation of the lithosphere [e.g. 37, 15]. To further reduce the model space dimensions being search, it is also necessary to make simplifying assumptions about the nature of afterslip. For example, one can assume a frictional model for afterslip and parameterize afterslip in terms of the unknown rheologic properties of the fault [e.g. 18, 20]. One can also assume that afterslip does not persist for more than a few months or a year and then model the later postseismic deformation assuming it to be the result of only viscoelastic relaxation [e.g. 34, 43]. However, postseismic afterslip in similar tectonic settings has been observed to persist for decades following earthquakes [4, 5]. Neglecting to allow for sustained afterslip as a postseismic mechanism could then lead to a biased inference of lithospheric viscosity. Indeed, the preferred viscoelastic model from Pollitz et al. [34] significantly underestimates near-field deformation, which could be indicative of unmodeled continued afterslip.

In this study, we assume that both afterslip and viscoelastic relaxation can contribute to postseismic deformation. Modeling both of these mechanisms creates a high dimensional model space that must be searched with nonlinear optimization methods. We first develop an initial postseismic model using the method described in Hines and Hetland [16]. This method simultaneously estimate the afterslip and effective lithospheric viscosity structure necessary to describe the first 0.8 years of postseismic deformation following the El Mayor-Cucapah earthquake. We then use the inferred effective viscosity structure to create a suite of postseismic models which are tested against available five years of postseismic data. Of the suite of models tested, we find that postseismic deformation following the El Mayor-Cucapah earthquake can be explained with a combination of sustained afterslip beneath the Sierra Cucapah and a Zener rheology upper mantle with a transient viscosity that decays from 5×10^{18} Pa s at 30 km depth to 1×10^{18} Pa s at 120 km depth.

2. Data Processing

We use continuous GPS position time series provided by University Navstar Consortium (UNAVCO) for stations within a 400 km radius about the El Mayor-Cucapah epicenter. We describe the coseismic and postseismic displacement resulting from the El Mayor-Cucapah earthquake collectively as $u_{\mathrm{post}}(t)$ and we consider the GPS position time series, $u_{\mathrm{obs}}(t)$, to be the superposition of $u_{\mathrm{post}}(t)$, secular tectonic deformation, annual and semi-annual oscillations, and coseismic offsets from significant earthquakes over the time span of this study. The June 14, 2010, Mw5.8 Ocotillo earthquake and the Brawley swarm, which included an Mw5.5 and an Mw5.3 event on August 26, 2012, (figure 1) are the only earthquakes that produced noticeable displacements in any of

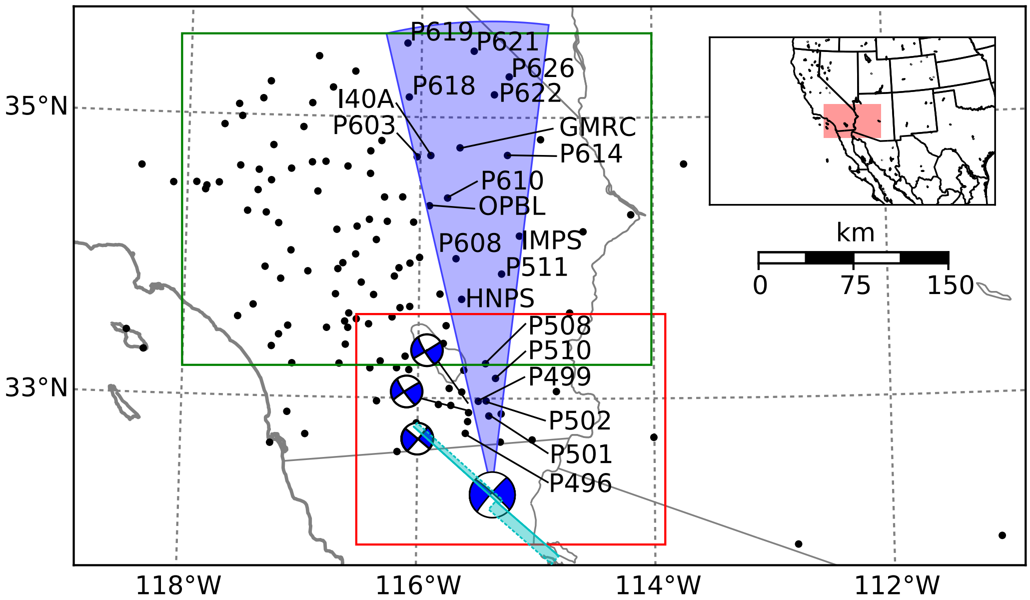

Figure 1: Map of the area where postseismic deformation following the El Mayor-Cucapah earthquake can be observed geodetically. The large focal mechanism is for the El Mayor Cucapah earthquake and the three small focal mechanisms are for the Octotillo earthquake and the two main shocks during the Brawley swarm. The black dots indicate the locations of GPS stations used in this study. The fault geometry used in this study is shown in cyan where dashed lines indicate buried edges of the fault segments. The green and red boxes denote the extent of the near and far-field displacement maps. The blue sector highlights the area within 10° of the El Mayor-Cucapah P axis and stations within this sector are used in the record sections in figures 8 and 14

the GPS position timeseries. We treat the displacements resulting from the Brawley swarm as a single event because the position time series are provided by UNAVCO as daily solutions. Although the Ocotillo earthquake had its own series of aftershocks [12], neither the Ocotillo earthquake nor the Brawley swarm produced detectable postseismic deformation and we model displacements resulting from these events with a Heaviside function, $H(t)$. We then model $u_{\mathrm{obs}}(t)$ as

$$u_{\mathrm{obs}}(t) = u_{\mathrm{pred}}(t) + \epsilon \tag{1}$$

where

$$\begin{aligned} u_{\mathrm{pred}}(t) = & u_{\mathrm{post}}(t)H(t - t_{\mathrm{emc}}) + c_0 + c_1 t + \\ & c_2 \sin(2\pi t) + c_3 \cos(2\pi t) + c_4 \sin(4\pi t) + c_5 \cos(4\pi t) + \\ & c_6 H(t - t_{\mathrm{oc}}) + c_7 H(t - t_{\mathrm{bs}}). \end{aligned} \tag{2}$$

In the above equations, t_{emc}, t_{oc} and t_{bs} are the times of the El Mayor-Cucapah earthuqake, Ocotillo earthquake, and the Brawley swarm, respectively, c_0 through c_7 are unknown coefficients, and ϵ is the observation noise. We only estimate jumps associated with the Ocotillo earthquake and Brawley swarm for stations within 40 km of their epicenters.

Stations which recorded displacements that clearly cannot be described by the aforementioned processes are not included in our analysis. This includes stations in the Los Angeles basin, where anthropogenic deformation can be larger than the postseismic signal that we are trying to estimate [3, 2] . In order to ensure an accurate estimation of the secular deformation, we only use stations that were installed at least six months prior to El Mayor-Cucapah earthquake. Several GPS stations were installed after the El Mayor-Cucapah earthquake to improve the spatial resolution of postseismic deformation [43] and it would be possible to subtract secular velocities derived from elastic block models [e.g. 28] from velocities recorded at the newly installed stations to get an estimate of postseismic velocities. However, we use coseismic and postseismic displacements, rather than velocities, in our inverse method described in Section 3. We use displacements because estimating velocities from an already noisy displacement time series can introduce significant aleatoric and epistemic uncertanties depending on exactly how the estimation is done (REF). This modeling choice prevents us from using the newly installed stations in Baja California in our analysis.

The October 16, 1999, Mw7.1 Hector Mine earthquake, which occurred about 270 km north of the El Mayor-Cucapah epicenter, produced transient postseismic deformation which we do not wish to model, either mechanically or through empirical line fitting. We thus restrict our analysis to deformation observed six years after the Hector Mine earthquake, which is when postseismic velocities at sites proximal to the Hector Mine epicenter are approximately constant [40]. When appraising our model fit in Section 3, we see some systematic residuals in the vicinity of the Hector Mine epicenter, which may be the result of errors in the assumption that the trend in Hector Mine postseismic deformation is linear after six years.

Studies of postseismic deformation typically assume a parametric form for $u_{\mathrm{post}}(t)$, such as one with a logarithmic or exponential time dependence [e.g. 41]. However, by assuming a logarithmic or exponential form of $u_{\mathrm{post}}(t)$ we run the risk of over fitting the GPS time series and inferring a nonexistent postseismic signal. We therefore do not assume any parametric form for $u_{\mathrm{post}}(t)$ and rather treat it as integrated Brownian motion, so that

$$\dot{u}_{\mathrm{post}}(t) = \sigma^2 \int_0^t w(s)ds, \tag{3}$$

where $w(t)$ is white noise and the variance of $\dot{u}_{\mathrm{post}}(t)$ increases linearly with time by a factor of σ^2. We use a Kalman filtering approach to estimate $u_{\mathrm{post}}(t)$ and the unknown parameters in eq. 2. In the context of Kalman filtering, our time varying state vector is

$$\mathbf{X}(t) = [u_{\mathrm{post}}(t), \dot{u}_{\mathrm{post}}(t), c_0, ..., c_7] \tag{4}$$

and eq. 2 is the observation function which maps the state vector to the GPS observations. We initiate the Kalman filter by assuming a prior estimate of $\mathbf{X}(t)$ at the first time epoch, denoted $\mathbf{X}_{1|0}$, which has a sufficiently large covariance, denoted $\mathbf{\Sigma}_{1|0}$, to effectively make our prior uninformed. For each time epoch, t_i, Bayesian linear regression is used to incorporate GPS derived estimates of displacement with our prior estimate of the state, $\mathbf{X}_{i|i-1}$, to form a posterior estimate of the state, $\mathbf{X}_{i|i}$, which has covariance $\mathbf{\Sigma}_{i|i}$.

We then use the posterior estimate of the state at time t_i to form a prior estimate of the state at time t_{i+1} through the transition function

$$\mathbf{X}_{i+1|i} = \mathbf{F}_{i+1}\mathbf{X}_{i|i} + \delta_{i+1} \tag{5}$$

where

$$\mathbf{F}_{i+1} = \begin{bmatrix} 1 & (t_{i+1} - t_i) & \mathbf{0} \\ 0 & 1 & \mathbf{0} \\ \mathbf{0} & \mathbf{0} & \mathbf{I} \end{bmatrix} \tag{6}$$

and δ_{i+1} is the process noise, which has zero mean and covariance described by

$$\mathbf{Q}_{i+1} = \sigma^2 \begin{bmatrix} \frac{(t_{i+1}-t_i)^3}{3} & \frac{(t_{i+1}-t_i)^2}{2} & \mathbf{0} \\ \frac{(t_{i+1}-t_i)^2}{2} & (t_{i+1} - t_i) & \mathbf{0} \\ \mathbf{0} & \mathbf{0} & \mathbf{0} \end{bmatrix}. \tag{7}$$

The covariance of the new prior state, $\mathbf{X}_{i+1|i}$, is then described by

$$\mathbf{\Sigma}_{i+1|i} = \mathbf{F}_{i+1}\mathbf{\Sigma}_{i|i}\mathbf{F}_{i+1}^T + \mathbf{Q}_{i+1}. \tag{8}$$

This process is repeated for each of the N time epochs at which point we use Rauch-Tung-Striebel smoothing [36] to find $\mathbf{X}_{i|N}$, which is an estimate of the state at time t_i that incorporates GPS observation for all N time epochs. Our final estimates of $u_{\mathrm{post}}(t)$ are used in subsequent analysis, while the remaining components of the state vector are considered nuisance parameters. In the interests of computational tractability, we down sample our smoothed time series from daily solutions down to weekly solutions.

The smoothness of $u_{\mathrm{post}}(t)$ is controlled by the chosen value of σ^2, which describes how rapidly we expect postseismic displacements to vary over time. Setting σ^2 equal to zero will effectively result in modeling $u_{\mathrm{post}}(t)$ as a straight line which is insufficient to describe the expected transient behaviour in postseismic deformation. The other end member, where σ^2 is infinitely large, will result in $u_{\mathrm{pred}}(t)$ overfitting the data. While one can use

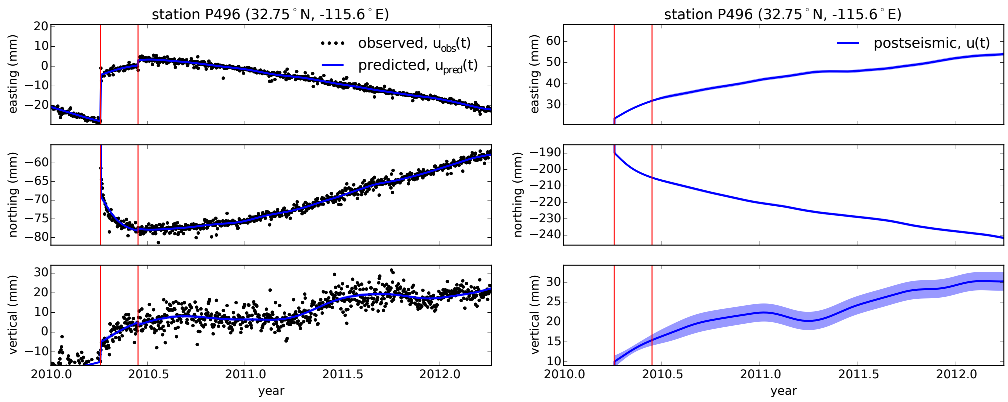

Figure 2:

a maximum likelihood based approach to picking σ^2 [e.g. 42], we rather take a subjective approach and choose a value for σ^2 that is just large enough to faithfully describe the observed deformation at the most near-field station in our study, P496, which exhibits the most pronounced rapid changes in velocity. This ensures that σ^2 will be sufficiently large so that our estimate of $u_{\text{post}}(t)$ does not smooth out potentially valuable postseismic signal at the remaining stations. We find that using $\sigma^2 = 0.05\text{m}^2/\text{yr}^3$ adequately describe all but the first week of postseismic deformation at station P496, which gets incorporated into our estimate of coseismic displacements (figure 2). By down sampling, we implicitly assume that the first week of deformation is overwhelmingly the result of afterslip and this afterslip is lumped into our estimates of coseismic slip. Figure 2 shows the estimate of coseismic and postseismic deformation, $u_{\text{post}}(t)$, for station P496 along with the estimated uncertainties. [10] noted that postseismic deformation can be observed at distances greater than 200 km from the Hector Mine earthquake and indeed, after filtering the time series for stations up to 400 km from the El Mayor-Cucapah epicenter, we also clearly see far reaching postseismic transient deformation (figure 3).

It is important to note that the shown uncertainties in $u_{\text{post}}(t)$ do not account for the non-negligible epistemic uncertainty in eq. 2. For example, we assume a constant rate of secular deformation, which appears to be an appropriate approximation for all but perhaps the stations closest to the Hector Mine epicenter, as noted aboved. Also, our model for seasonal deformation in eq. 2 assumes a constant amplitude over time, which means that any yearly variability in the climatic conditions could introduce systematic residuals [7]. Indeed, it would be more appropriate to consider the seasonal amplitudes $c_2 - c_5$ in eq. 2 as stochastic variables [29]. By using constant seasonal amplitudes our estimate of $u_{\text{post}}(t)$ seems to describe some of the unmodeled oscillations (e.g. figure 3).

We show in figures 4 and 5 the near and far-field postseismic deformation accumulated over the intervals 0-0.8 years, 0.8-3.0 years, and 3.0-5.0 years, as well as the coseismic displacements. In the far-field to the north, we can see south trending displacements for the first 3.0 years following the earthquake at stations as far as ∼400 km from of the El Mayor Cucapah epicenter. These displacements are most pronounced along the direction of the El Mayor-Cucapah P axis. A similar eastward trend can be seen in

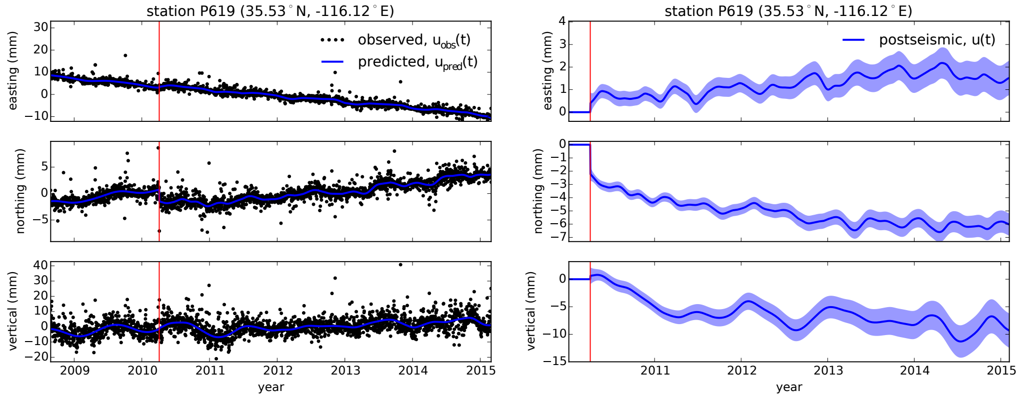

Figure 3:

the few far-field stations along the T axis in Arizona. After 3.0 years, The trend in far-field postseismic deformation is barely perceptible. The vertical deformation in the far-field is difficult to attribute to postseismic processes. Most far-field stations display an initial subsidence for the first year after the El Mayor-Cucapah earthquake followed by continued uplift. This trend in vertical deformation can be observed in all three of the quadrants where postseismic data is available, which means that the vertical deformation does not exhibit an anti-symetric quadrant pattern, as would be expected for postseismic processes. Although we use vertical deformation in our analysis in section 3, we do not put an emphasis on trying to describe the vertical deformation as it likely does not have postseismic origins.

The near-field postseismic deformation is notably sustained when compared to the far-field deformation. Namely, the station in this study which is closest to the El Mayor-Cucapah epicenter, P496, is moving at a steady rate of $\sim$ 1.4 cm/yr to the south five years after the El Mayor-Cucapah earthquake. Vertical postseismic deformation in the near-field does display a quadrant pattern which is consistent with the coseismic vertical deformation, suggesting that it is indeed resulting from tectonic processes. However, the vertical postseismic deformation signal is only apparent for the first year after the earthquake (figure 4). As with the far-field deformation, there is a general trend of uplift in the near-field one year after the earthquake which we do not consider to be related to postseismic processes.

3. Postseismic Modeling

In this paper, we seek to find the mechanisms driving five years of postseismic deformation following the El Mayor-Cucapah earthquake. We consider afterslip and viscoelastic relaxation in the lithosphere and asthenosphere as candidate mechanisms. Poroelastic rebound has also been used to model postseismic deformation [e.g. 21]; however, Gonzalez-Ortega et al. [11] suggest that any contribution to postseismic deformation from poroelastic rebound would be negligible. Furthermore, we consider stations which

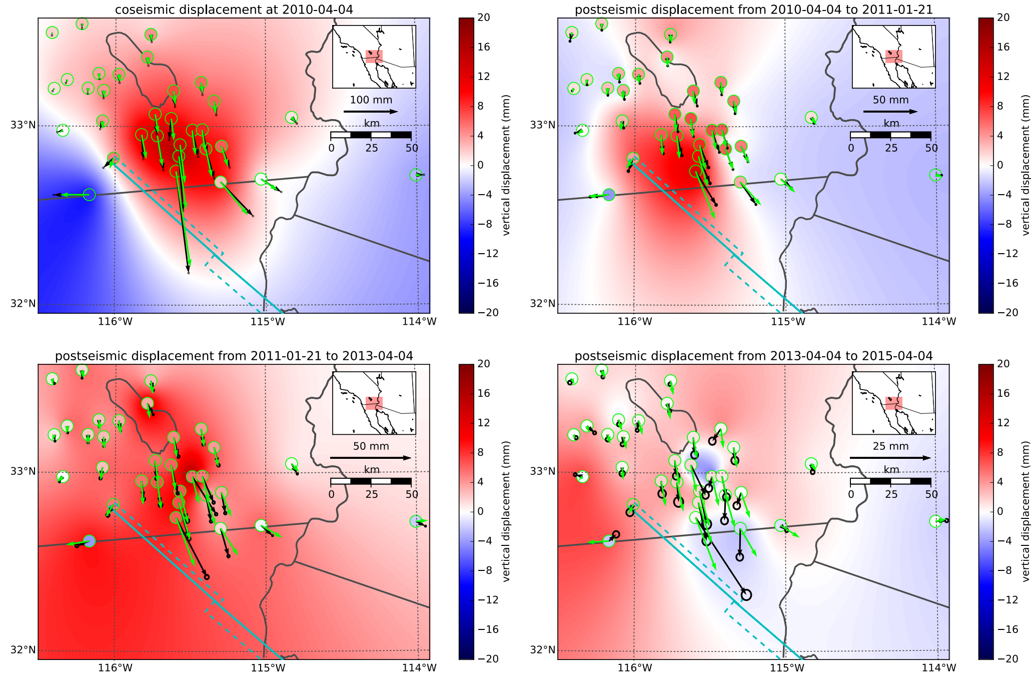

Figure 4:

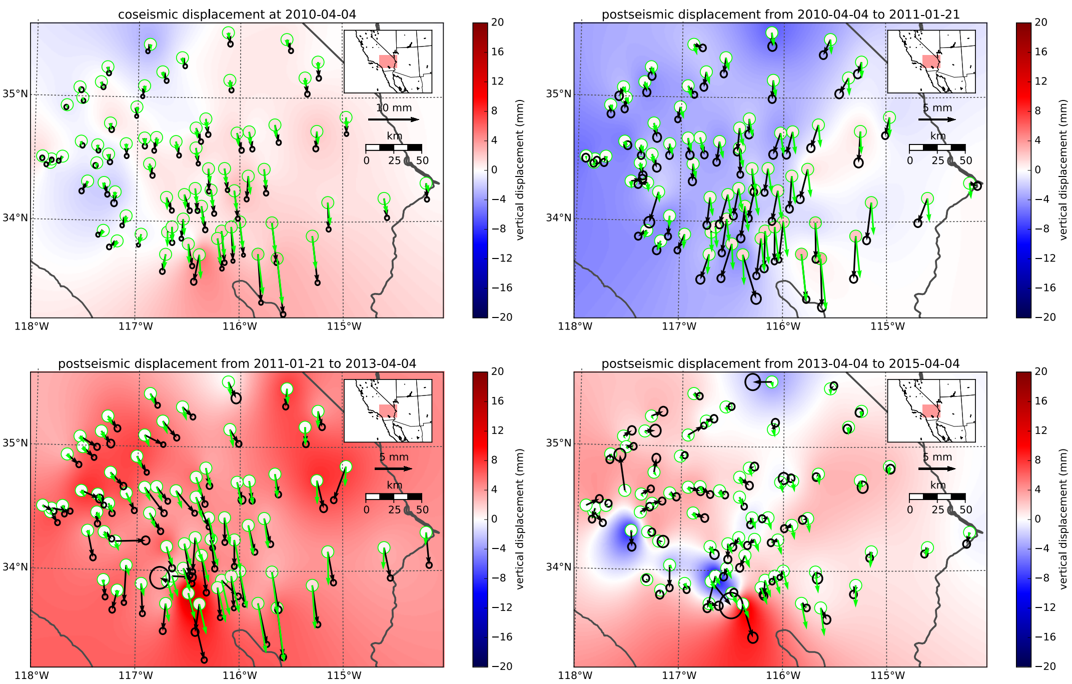

Figure 5:

depth (km)	λ (GPa)	μ (Gpa)	ρ (kg/m^3)	η_{eff} (10^{18} Pa s)	μ_{k}/μ
0-5	24.0	24.3	2400	-	-
5-15	35.2	35.4	2670	-	-
15-30	41.8	41.9	2800	44.3	0.0
30-60	61.0	60.8	3000	5.91	0.375
60-90	61.0	60.8	3000	1.99	0.375
90-120	61.0	60.8	3000	1.31	0.375
120-150	61.0	60.8	3000	1.10	0.375
150-∞	61.0	60.8	3000	1.07	0.375

Table 1: Assumed and estimated material properties. λ, μ, and ρ are assumed known *a priori*, η_{eff} is estimated in section 3.2 and μ_k/μ are the optimal shear moduli ratios found in section 3.3 for a Zener rheology.

are sufficiently far away from the main rupture that poroelastic rebound should be insignificant.

We estimate coseismic and time-dependent postseismic fault slip, both of which are assumed to occur on the fault geometry estimated by Wei et al. [46] with some modifications. Field studies [8] and LIDAR observations [31] have revealed a significantly more complicated fault geometry than what was inferred by Wei et al. [46], especially within the Sierra Cucapah. However, we find that a relatively simple coseismic fault geometry based on [46] is adequate because most of the stations used in this study are sufficiently far from the El Mayor-Cucapah rupture zone that they are insensitive to the details in the fault geometry found by Fletcher et al. [8] and Oskin et al. [31]. The fault geometry used in this study (figure 1) consists of the two main fault segments inferred by Wei et al. [46], where the northern segment runs through the Sierra Cucapah up to the US-Mexico border and the southern segment is the Indiviso fault which extends down to the Gulf of California. Both segments extend from the surface to 15 km depth. We extend the northern segment by 40 km to the northwest, motivated by the clustering of aftershocks on the northern tip of the coseismic rupture zone [12, 22]. This extended fault segment was also found to be necessary by Rollins et al. [38] and Pollitz et al. [34] in order to describe the postseismic deformation.

3.1. elastic inversion

We consider a variety of rheologic models for the lithosphere and asthenosphere. The simplest rheologic model is to consider the lithospere and asthenosphere to be effectively elastic and isotropic. In such case, the rheologic parameters consist of the Lamé parameters, λ and μ, which are reasonably well known and we use the values listed in table 3 throughout this paper. The values for λ and μ are consistent with the properties used in the coseismic model by [46] and the 1D SCEC velocity model. The only unknowns are then the distribution of fault slip, which can be easily estimated due to the linearity of the forward problem. Using a subset of the GPS stations considered in this study, Rollins et al. [38] found that postseismic deformation following the El Mayor-Cucapah earthquake can be explained with afterslip on the coseismic fault plane and they did not require any viscoelastic relaxation to describe the observations. We also perform an elastic slip inversion but we use GPS stations within a larger radius about the El Mayor-Cucapah epicenter (400 km instead of $\sim$200 km). Our forward problem describing predicted postseismic deformation u_{pred} in terms of time dependent fault slip s is

$$u_{\text{pred}}(x,t) = \int_F s(\xi,t)g(x,\xi)d\xi \tag{9}$$

where $g(x,\xi)$ is an elastic Green's function describing the displacement at position x resulting from a unit of slip at ξ on the fault, denoted by F. We estimate coseismic slip, as well as the rate of afterslip over time intervals spanning 0.0-0.125 years, 0.125-0.25 years, 0.5-1.0 years, and at 1.0 year intervals for the remaining five years. Each fault segment is discretized into roughly 4 km by 4 km patches and we estimate a strike-slip and thrust component of slip for each patch. We impose that the coseismic slip and rates of afterslip are within 45° of right-lateral slip. We also add zeroth order Tikhonov regularization so that our slip solution satisfies

$$\min_s \left(\left|\left| \frac{u_{\text{pred}}(s) - u_{\text{post}}}{\sigma_{\text{obs}}} \right|\right|_2^2 + \lambda_s ||s||_2^2 \right). \tag{10}$$

The penalty parameters, λ_s, is chosen with a trade-off curve.

Our coseismic and afterslip solutions are shown in figure (TBD). As with Rollins et al. [38], we find that a significant amount of afterslip on the southern segment is required to explain the observations. Figure (TBD) is a scaled record section of observed and predicted postseismic displacements for stations along the El Mayor-Cucapah P axis. It is evident from figure (TBD) that the near-field stations ($\lesssim$ 200 km) can be well described by afterslip in an entirely elastic medium while there is a systematic underestimation and inability to reproduce the transient deformation in the far-field stations ($\gtrsim$ 200 km). When the fault segments used in the inversion are extended down to 30 km depth, rather than 15 km, the systematic far-field residuals are smaller but remain apparent. In the following sections we seek to better describe the far-field postseismic deformation using viscoelastic models.

3.2. constraints on effective viscosity

For any linear viscoelastic rheology of the lithosphere and asthenosphere, postseismic displacement resulting from time dependent fault slip can be described as

$$u_{\text{pred}}(x,t) = \int_F s(\xi,t)g(x,\xi)d\xi + \int_0^t \int_F s(\xi,\tau)f(t-\tau,x,\xi)d\xi d\tau \tag{11}$$

where $f(t,x,\xi)$ describes the time-dependent velocity at x resulting from viscoelastic relaxation of stresses induced by slip at ξ. f is a function of λ, μ, and any additional rheologic parameters controlling the viscoelastic response, which are generally not well known. Schematic representations of the viscoelastic rheologic models considered in this study for the lower crust and upper mantle are shown in figure 6. We consider Maxwell viscoelasticity, where the steady state viscosity η_M is unknown, Zener viscoelasticty, where the transient viscosity η_K and transient shear modulus μ_K are unknown, and Burgers viscoelasticity, where η_M, η_K, and μ_K, are all unknown. We further discuss these rheologic models and their use in geophysical studies in the discussion.

In order to greatly simplify the inverse problem, we use the method described in Hines and Hetland [16] to constrain an initial effective lithospheric viscosity structure from

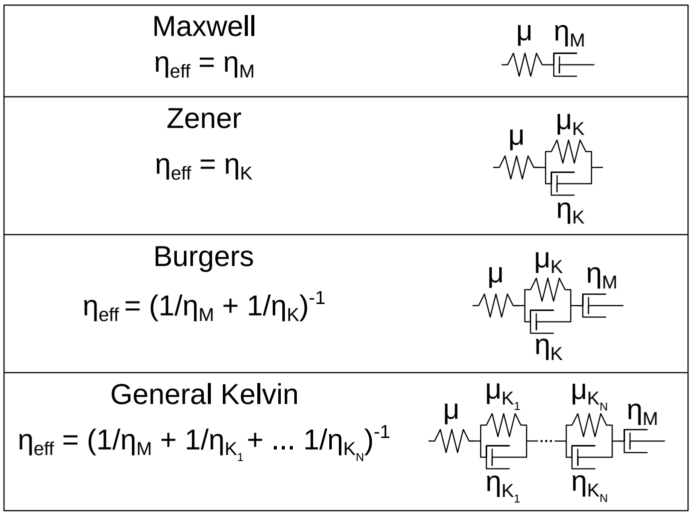

Figure 6:

the early postseismic deformation. The method relies upon the fact that immediately after an earthquake, stresses throughout the lithosphere and asthenosphere are only controlled by the relatively well known instantaneous elastic properties. This means that the rate of deformation in each parcel of the lithosphere will deform at a rate that is inversely proportional to its effective viscosity, $\eta_{\text{eff}} = \frac{\sigma}{\dot{\epsilon}}|_{t=0}$, and independent of η_{eff} elsewhere. Then, through linear superposition, we can deduce that the initial rate of surface deformation resulting from viscoelastic relaxation is a summation of the surface deformation resulting from each parcel, scaled by the reciprocal of the parcel's viscosity. That is to say

$$f(0,x,\xi) = \int_L \frac{h(x,\xi,\zeta)}{\eta_{\text{eff}}(\zeta)} d\zeta, \tag{12}$$

where $h(x,\xi,\zeta)$ describes the initial rate of deformation resultion from viscoelastic relaxation at ζ induced by slip at ξ and L denotes the lithosphere and asthenosphere. We can combine eq. 12 with 11 to get a first order approximation for early postseismic deformation,

$$u_{\text{pred}}(x,t) \approx \int_F s(\xi,t)g(x,\xi)d\xi + \int_0^t \int_F \int_L \frac{s(\tau,\xi)}{\eta_{\text{eff}}(\zeta)} h(x,\xi,\zeta) d\zeta d\xi d\tau, \tag{13}$$

which is valid for as long as the rate of deformation resulting from viscoelastic relaxation is approximately constant. Although eq. (13) may only be valid for a short portion of the postseismic period, its utility becomes apparent when noting that g and h are only functions of the fault geometry and instantaneous elastic properties, λ and μ, and so g and h can be computed numerically as a preprocessing step and the forward problem in eq. (13) can be rapidly evaluated for any realization of s and η_{eff}. This is in contrast to evaluating the full forward problem, eq. (11), numerically for each realization of s and unknown rheologic properties. Figure 6 shows how estimates of η_{eff} can then be used as a constraint on the unknown parameters for various linear viscoelastic rheologies.

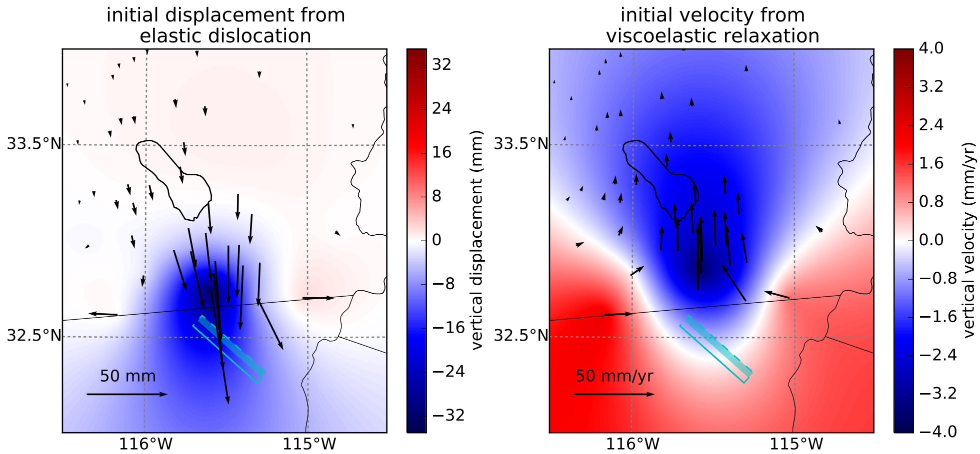

Figure 7: afterslip and viscoelastic relaxation in lower crust

We perform an initial inversion of postseismic displacements using the approximation in eq. 13. We estimate coseismic slip and afterslip with the same spatial and temporal discretization as in section 3.1. Simultaneously, we estimate η_{eff} within six vertically stratified layers which have depths ranging from 15-30 km, 30-60 km, 60-90 km, 90-120 km, 120-150 km, and 150 km to the bottom of our numerical model domain at 800 km. We again restrict fault slip to occur between 0 and 15 km depth and we made this choice to help eliminate inevitable non uniqueness. It has long been recognized that fault slip at sufficiently great depths can produce surface deformation that is indistinguishable from viscoelastic relaxation, at least in two-dimensional models [39]. Since we are trying to simultaneously model these two processes, it is necessary to put sensible constraints on the depth of fault slip. Additionally, we note that when simultaneously estimating afterslip in the lower crust and a lower crustal viscosity, the inverse problem becomes particularly ill-posed. This ill-posedness is illustrated in figure (7), which shows the displacement resulting from a meter of slip on a fault extending from 15 to 30 km depth as well as the initial velocity resulting from viscoelastic relaxation in the lower crust, which is given a viscosity of 10^{18} Pa s. The horizontal displacement from fault slip is in the opposite direction as the displacements resulting from subsequent viscoelastic relaxation. This means that surface displacements resulting from afterslip at lower crustal depths can be cancelled out, at least partially, by a low viscosity lower crust. We eliminate this null space by allowing only one mechanism in the lower crust, which we choose to be viscoelastic relaxation. This is not to say that we do not believe deep afterslip to be a possibility, rather we restrict slip to seismogenic depths as a modeling necessity. Although, it has been noted that the pattern of vertical postseismic deformation following the El Mayor-Cucpah earthquake indicates that a significant amount of afterslip must be shallow [38].

Further details of how s and η_{eff} are estimated from postseismic deformation can be found in Hines and Hetland [16]. We note that a nonlinear Kalman filter based inverse method can be used to estimate s and η_{eff} in a manner akin to Segall and Mathews

[42] or McGuire and Segall [27], in which we would not have to explicitly impose a time dependent parameterization of s. We have thoroughly explored Kalman filter based approaches, but we ultimately prefer the method described in Hines and Hetland [16] because of its relative simplicity. Moreover, we believe the piecewise continuous respresentation of slip with respect to time to be sufficiently general for the respoving power of these GPS data.

The first step in our inverse method is to determine at which point the early postseismic approximation, eq. 13 breaks down, which we will denote as t_{bd}. As noted, it is valid for approximately as long as the rate of deformation resulting from viscoelastic relaxation is approximately constant. We can almost certainly assume that deformation at the most far-field stations, which are ~ 400 km away from the El Mayor-Cucapah epicenter, is the result of viscoelastic relaxation. The approximation should then be valid for as long as a linear trend adequately approximates the far-field deformation. Using this logic, it would appear that $t_{\mathrm{bd}} \approx 1$ year after the El Mayor-Cucapah earthquake. Another way to determine t_{bd} is to find the best fitting prediction of eq. 13 to observed deformation using increasing durations of the postseismic timeseries. t_{bd} should be the point when eq. 13 is no longer capable of describing the observed deformation without incurring systematic misfits. This is illustrated in figure 8, which show the scaled radial components of displacement for stations along the El Mayor-Cucapah P axis. When using eq. 13 to fit the entire five years of postseismic displacement we see that the near-field displacements, eg. station P501, are accurately predicted but when looking at displacement in the far-field, eg. station P621, we see that eq. 13 overestimates the rate of deformation in the later postseismic and underestimates the rate of deformation in the early period. Due to the low signal-to-noise ratios for far-field stations, it is difficult to determine at what point eq. 13 is no longer able to predict the observed displacements without incurring any significant systematic misfit; however, we settle on $t_{\mathrm{bd}} = 0.8$ years after the earthquake, while acknowledging that the choice is subjective. As noted in [16], overestimating t_{bd} will result in a bias towards overestimating η_{eff}, while picking a t_{bd} which is too low will not necessarily result in a biased estimate of η_{eff}; although the uncertainties would be larger. We can then consider our subsequent inferences of η_{eff} to be an upper bound on the lithospheric strength needed to describe the far-field rate of deformation during the first 0.8 years of postseismic deformation.

We estimate coseismic slip, afterslip, and effective viscosity by solving

$$\min_{s,\eta_{\mathrm{eff}}} \left(\left|\left| \frac{u_{\mathrm{pred}}(s, \eta_{\mathrm{eff}}) - u_{\mathrm{obs}}}{\sigma_{\mathrm{obs}}} \right|\right|_2^2 + \lambda_s ||s||_2^2 + \lambda_\eta ||\nabla \eta_{\mathrm{eff}}^{-1}||_2^2 \right) \tag{14}$$

where u_{obs} consists of the first 0.8 years of postseismic deformation and u_{pred} are the predicted displacements from eq. 13. Due to inherent nonuniqueness, we have added zeroth order Tikhonov regularization to estimates of s, and second order Tikhonov regularization to estimates of effective fluidity, $\eta_{\mathrm{eff}}^{-}1$. The degree to which we impose the regularization on slip and viscosity is controlled by the penalty parameters λ_s and λ_η. The penalty parameters are chosen with two trade-off curves. We first choose λ_s while fixing λ_η at 0 and then λ_η is determined while fixing λ_s at the chosen value. We note that our goal here is to get a prior constraint on η_{eff} to minimize the amount of searching we have to do when describing the postseismic deformation over the full five years, which we do in section 3.3. Estimates of s made here will not be used in section 3.3, and so

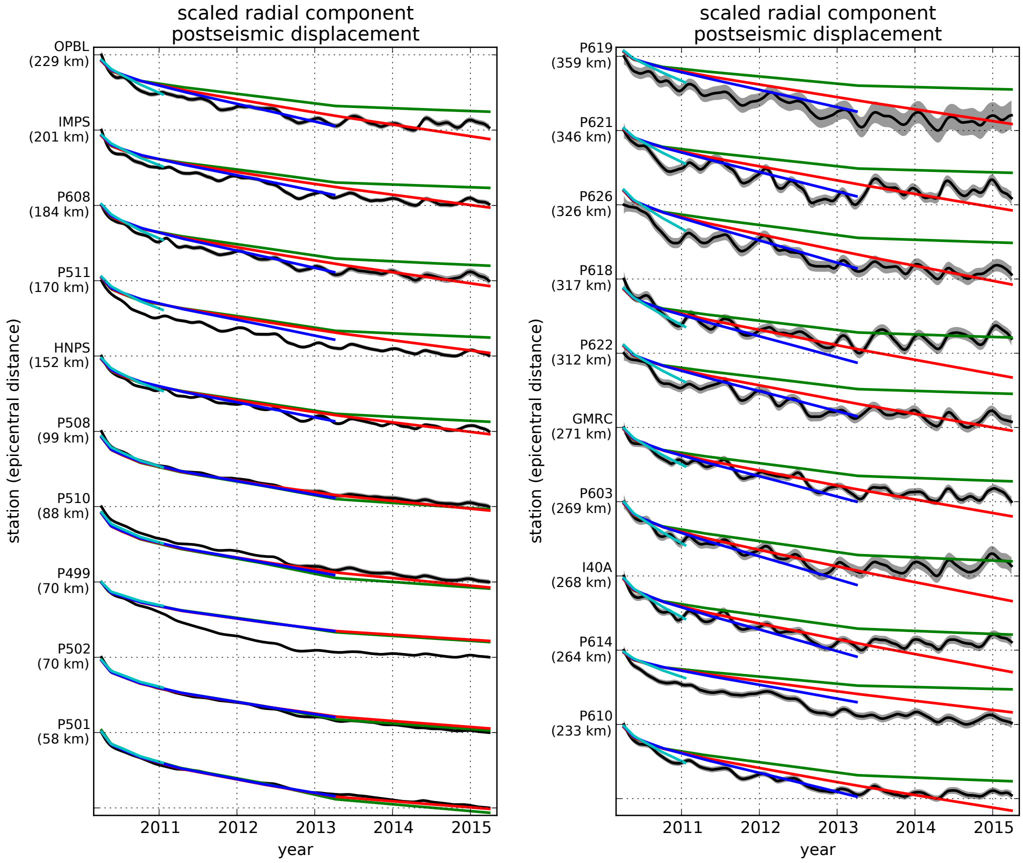

Figure 8: record section

the motivation behind even adding regularization to s is to ensure that the slip driving viscoelastic relaxation in eq. 13 is sensible.

Our inferred estimates of effective viscosities, and corresponding fluidities, are shown in figure 9 with their 95% confidence intervals indicated, which were inferred through bootstrapping. Although fluidity is rarely used in geophysical literature, it is more natural to consider fludities rather than viscosities since eq. 12 is linear with respect to fluidity and so the fluidity is proportional to the amplitude of the viscoelastic signal coming from each discretized layer of the lithosphere and asthenosphere. We note that the magnitude of the uncertainties on viscosity tend to decrease as we increase λ_η. Our choice our λ_η was based on a standard technique used in geophysical inverse problems which has no statistical backing. It is therefore difficult to interpret the magnitude of uncertainties on viscosities shown in figure 9; although, we do believe that the relative uncertainty between layers is accurately depicted. The uncertainties in fluidities increases with depth, as would be expected due to decreased sensitivity with depth. Nevertheless, a robust feature that we see is that the viscosity below 60 km depth needs to be on order of 10^{18} Pa s to describe the early rate of postseismic deformation at far-field stations. Our inference that the lower crust and mantle from 30 to 60 km depth are appreciable stronger than the underlying mantle is consistent with the range of lithosphere-asthenosphere boundary depths inferred by Lekic et al. [23]. The viscosity of the lower crust is the least well constrained as there is no evidence of relaxation in that layer, meaning that the viscosity is effectively infinite during the first 0.8 years after the El Mayor-Cucapah earthquake. Our inference of a mantle viscosity on the order of 10^{18} Pa s and a relatively stronger lower crust is consistent with the inferred steady-state viscosities from Pollitz et al. [35], Pollitz [33], Johnson et al. [19], Spinler et al. [43], and Rollins et al. [38].

Our initial estimate for coseismic slip and cumulative afterslip over the first 0.8 years after the El Mayor-Cucapah earthquake are shown in figure 11. To show how our slip solution is influenced by allowing for a viscoelastic lithopshere, we also show the coseismic slip and afterslip inferred using the same geometry, discretization, and regularization, but we assume the lithosphere and asthenosphere are elastic. In both coseismic inversions, most of the slip is inferred to be in the Sierra Cucapah and is right lateral with a significant normal component. This is consistent with field studies, [8] as well as the coseismic slip from [46]. The potency of inferred coseismic slip is $3.32 \times 10^9\text{m}^3$, which is equivalent to a moment magnitude of 7.28 when assuming a shear modulus of 32 GPa. The potency of the inferred coseismic slip model when assuming an elastic lithosphere is not significantly different, $3.55 \times 10^9\text{m}^3$. The striking difference between the two models is that the inferred afterslip on the Indiviso fault segment is significantly larger when not accounting for viscoelasticity. The potency of afterslip in the elastic model is $2.7 \times 10^9\text{m}^3$, compared to $0.85 \times 10^9\text{m}^3$ for the viscoelastic model. The former is comparable to the size of the mainshock which, as noted by [38], is implausibly large. The significant amount of afterslip inferred to be on the Indiviso fault by [38] seems to be compensating for unmodeled viscoelastic relaxation at depths greater than 60 km. The fact that there is still an appreciable amount of deep afterslip inferred on the Indiviso fault even when allowing for viscoelastic relaxation in the lower crust and upper mantle raises the question of whether it is compensating for viscoelastic relaxation that is more localized than we allow for since we only estimate depth dependent variations in viscosity.

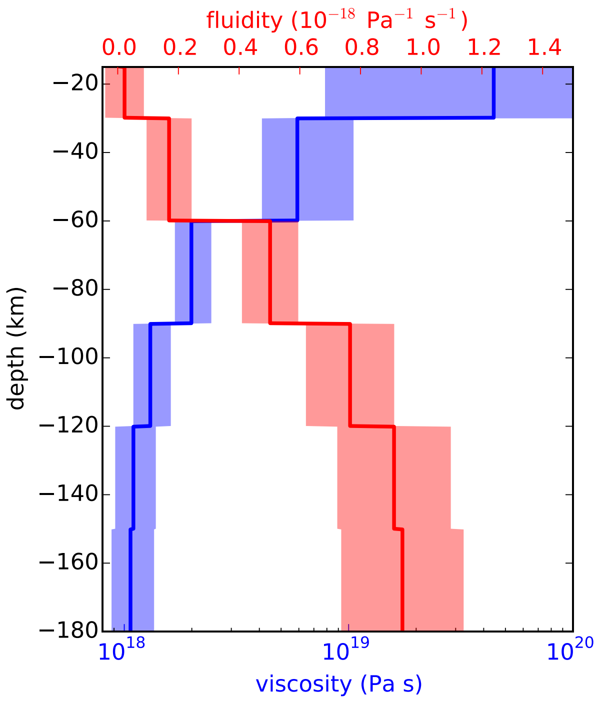

Figure 9: effective viscosity

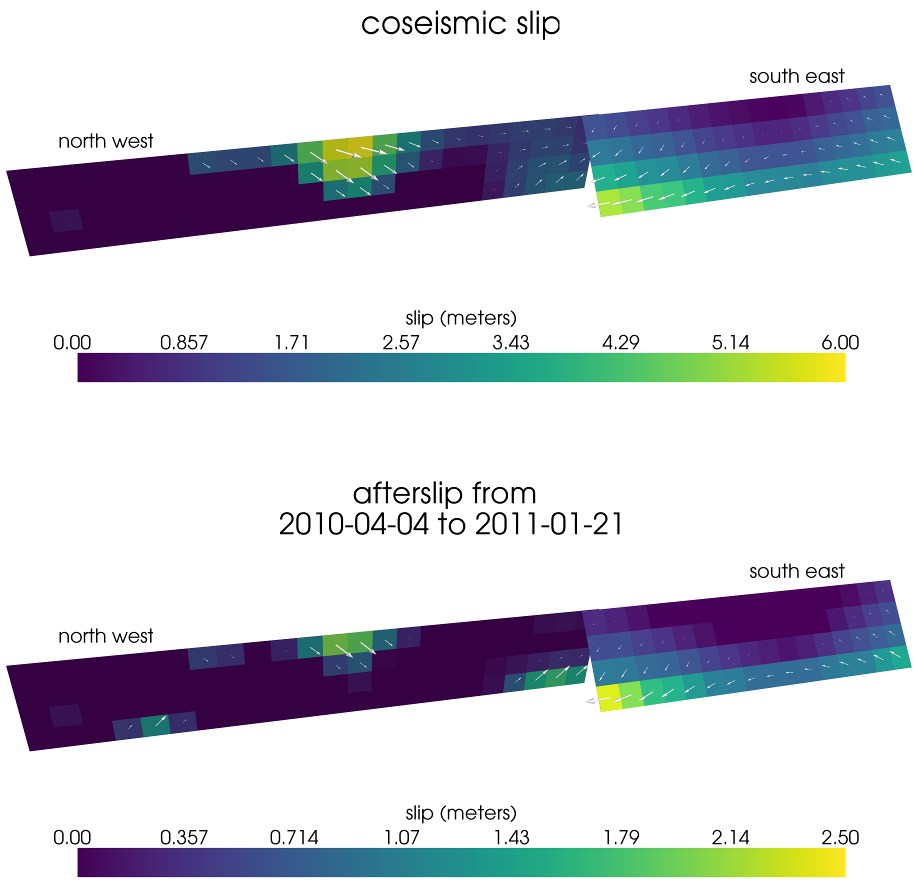
coseismic slip
south east
north west
slip (meters)
0.00
0.857
1.71
2.57
3.43
4.29
5.14
6.00
afterslip from
2010-04-04 to 2011-01-21
south east
north west
slip (meters)
0.00
0.357
0.714
1.07
1.43
1.79
2.14
2.50

Figure 10:

3.3. Full Inversion

In the previous section we used the efficient inverse method described by [16] to constrain the effective lithospheric viscosity required to explain the first 0.8 years of postseismic deformation. In this section we use the inferred effective lithospheric viscosities as a prior constraint when searching for rheologic models of the lithosphere which are capable of describing the available five years of postseismic data.

Figure 6 describes how the inferred effective viscosities from section 3.2 constrain the rheologic parameters for various assumed rheologic models. In this section we perform a series of inversions where we estimate the coseismic slip and afterslip assuming a variety of lithospheric rheologies which are consistent with our findings from 3.2. Our forward problem is now eq. 11 rather than the approximation given by eq. 13. As a reference, we compare the best fit solution for each assumed lithospheric model to a the best fit solution assuming an entirely elastic lithosphere. One intuitive criterion for a viscoelastic lithospheric model to be plausible is that it should be able to predict observable deformation better than a lithospheric model which is elastic.

We first assume that the crust and mantle can be described with a Maxwell rheology, and so inferences of η_{eff} are equivalent to inferences of η_{M}. We compute f and g from eq. 11 using Pylith [1] and assume the same spatial and temporal discretization of s as in section 3.2. The misfit for the Maxwell model, defined by eq. **??**, is 62.0 which is significantly higher than that of the elastic model, 47.5. As noted, our estimates of η_{eff} can be thought of as an upper limit, and we have tried using viscoelastic Green's functions, f, with lower viscosities but that only increases the misfit. It is apparent that most of the misfit comes from the Maxwell model significantly overestimating the rate of deformation after ~ 3 years following the earthquake. Although, numerous studies have described postseismic deformation in Southern California using a Maxwell viscoelastic rheology with viscosities consistent with ours, it is clear that such a model is incapable of describing the entire postseismic time series. As previously noted, [32], recognized this deficiency in a Maxwell rheology which motivated their exploration of a Burgers rheology upper mantle [33].

Rather than exploring a Burgers rheology mantle, which introduces two new parameters that need to be estimated, η_K and μ_K, we first consider a Zener rheology for the mantle, which only introduces the unknown parameter μ_k. We assume that the lower crust still has a Maxwell rheology. The steady state viscosity, η_M, in the crust and the transient viscosity, η_{K}, in the mantle are set equal to the inferred effective viscosities. The unknown rheologic parameter which we estimate is the ratio of shear moduli, $\nu = \frac{\mu_K}{\mu_M}$. We compute nine different sets of Green's functions, f and g, using Pylith where we assume different values of ν ranging from 0 to 1. The former being a degenerate case when the Zener model becomes the Maxwell model from above and the later being a Jeffreys solid. We estimate coseismic slip and afterslip for each realization of ν. The misfit as a function of ν is shown in figure 12. The optimal value of ν is found to be 0.375, which has a misfit of 44.9, which seems like a modest improvement from the elastic model; however, the improvement can be clearly seen in the fit to the far-field data which does a significantly better job at explaining the rate of deformation throughout the 5 years (figure 14). This significant improvement is seen for all shear modulus ratios greater than about 0.125.

Because we are able to adequately describe the available five years of postseismic seismic deformation with a Zener model, we do not find it necessary to explore the parameter space for a more complicated Burgers rheology. However, since the Zener model can be thought of as the limit when the steady state viscosity in a Burgers rheology is infinite, we can conclude that any Burgers rheology that has a transient viscosity consistent with that found in 3.2 and an effectively infinite steady state viscosity on the timescale of five years, $> 10^{20}$ Pa s, would also be able to satisfactorily describe the observable postseismic deformation.

Satisfied with a Zener rheology for the mantle with shear modulus ratio of 0.375, our final step is to choose a damping parameter for out estimates of coseismic slip and afterslip, which has been fixed at 0 until now. We estimate the damping parameter, again enforcing smallness on our model, using another L-curve test. Our preferred model for coseismic slip and afterslip is shown in figure 13.

The postseismic displacements predicted for our preferred slip model and rheologic model of the lithospheric are shown in figures 4 and 5 as well as 14. Additionally, we show the predicted postseismic deformation broken down into an elastic and viscoelastic component (figure (TBD)). Overall, the trend in the near-field and far-field transient deformation is accurately described by our preferred model. In particular, the trend in far-field deformation is much better described by our preferred model, which has a Zener rheology mantle, than either an elastic model or a model with a Maxwell viscoelastic mantle (figure 14). There are a few areas where we have notable misfit. Most of our misfit is for the near-field stations in the Imperial Valley and we attribute this misfit to our relatively simple fault geometry, which does not account for fault slip in the Imperial Valley triggered by the El Mayor earthquake [45, 44]. Additionally, we see systematic misfit in the later postseismic period west of the location of the Landers and Hector Mine earthquakes, which may be the result of unmodeled postseismic deformation resulting from those earthquakes. Lastly, there are clear discrepancies between the observed and predicted vertical deformation following the first year after the El Mayor Cucapah earthquake. We observe a general uplift throughout Southern California, which is inconsistent with any postseismic model, which would produce a quadrant pattern of deformation.

The cumulative potency of slip over time is shown in figure (TBD). The inferred coseismic potency is $3.1 \times 10^9\text{m}^3$, equivalent to a Mw7.26 earthquake, and the potency of five years of afterslip is $1.2 \times 10^9\text{m}^3$. While most of the afterslip is inferred to be within the first couple months of the earthquake, accounting for the most rapid near-field transient deformation, we infer that afterslip in the vicinity of the Sierra Cucapah, where most slip occurred during the main shock, is necessary to explain the sustained rate of deformation in the near-field. We emphasize, that the GPS station closest to where we infer there to be sustained afterslip, P496, is still about 30 km away, which we believe is too distil for us to conclusively argue for sustained brittle deformation rather ductile deformation in a shear zone, especially for the last two years where afterslip is inferred to be on the deepest patches. Although we do note that it is not unheard of for afterslip to persists for years or decades following an earthquake [4]. Either way, we can conclusively say a localized deformation mechanism is required to explain the available five years of near-field deformation.

4. Discussion

Most postseismic studies assume Maxwell viscoelasticity in the lower crust and upper mantle, which is the simplest viscoelastic rheologic model [e.g. 30, 35, 14, 9, 18, 13]. In

Southern California, postseismic studies following the Landers [35], Hector Mine [32], and El Mayor-Cucuapah earthquake [43, 38], have assumed Maxwell viscoelasticity in the lithosphere and asthenosphere and have inferred upper mantle viscosities ranging from 10^{17} to 10^{18} Pa s with a relatively stronger lower crust. Our inference that the the crust and uppermost mantle are relatively strong compared to the underlying mantle is also consistent with that found by Freed et al. [10]. While these inferences are consistent with our effective viscosities, they are inconsistent with viscosity estimates made from geophysical processes that occur over longer time scales. Studies on interseismic deformation [25] and lake loading [26], which are both processes that occur on the timescale of 10^2 years, infer a Maxwell viscoelastic upper mantle with a viscosity on the order of 10^{19} Pa s.

An additional deficiency in the Maxwell rheology is that it predicts a steady decay over time in the rate of postseismic deformation, which fails to describe the commonly observed rapid early transience followed by a relatively steady rate postseismic deformation. One could explain the early transient postseismic deformation with fault creep and the later phase with relaxation in a Maxwell viscoelastic lower crust and upper mantle [e.g 13, 18]. However, the trend in postseismic deformation at distances greater than about 200 km from the El Mayor Cucapah epicenter, which can only be attributed to viscoelastic relaxation [10], cannot be explained with a Maxwell viscoelastic lithosphere (figure 14).

We found that a Zener rheology in the upper mantle with a transient viscosity of about 10^{18} Pa s does a noticeably better job at predicting far-field postseismic deformation. A generalization of the Zener viscoelastic model, consisting of several Kelvin elements connected in series, is commonly used to describe the spectrum of frequencies where seismic attenuation is observed [24]. The highest viscosity needed to describe attenuation of earth's lowest frequency normal modes is on the order of 10^{16} Pa s [47] and the largest characteristic relaxation time would be on the order of days. Even though our inferred transient viscosity is orders of magnitude larger than that required for seismic attenuation models, the two models are not incompatible. Rather the delayed elasticity in seismic attenuation models occurs on such short time scales that it can be considered part of the instantaneous elastic phase of deformation associated with the preferred Zener model in this study.

Of course, it has long been recognized that a Zener rheology provides an incomplete descriptions of the asthenosphere, as it does not have the fluid behaviour required for mantle dynamics on geologic time scales. Yuen and Peltier [47] proposed a Burgers rheology with a low viscosity ($\approx 10^{16}$ Pa s) in the Kelvin element and high viscosity ($\approx 10^{21}$ Pa s) in the Maxwell element which is capable of describing both seismic attenuation and the fluid-like behaviour required for glacial isostatic rebound and mantle convection. The justification of a Burger's rheology mantle is further supported by laboratory experiments on the strength of olivine [6]. Pollitz [33] sought to describe postseismic deformation following Hector Mine with a Burgers rheology mantle and they found a best fitting transient viscosity of 1.6×10^{17} Pa s and steady state viscosity of 4.6×10^{18} Pa s. While the Burgers rheology was introduced as a means of bridging to gap between relaxation observed in long and short term geophysical processes, the inferred steady state viscosity from Pollitz [33] is still inconsistent with the Maxwell viscosities inferred from Lundgren et al. [25] and Luttrell et al. [26]. Additionally, the transient viscosity inferred by Pollitz [33] is needed to describe the earliest phase of postseismic deformation following the Hector Mine earthquake, which may be the result of shallow afterslip. While Pollitz [33] ruled out deep afterslip as an alternative mechanism based on inconsistent vertical deformation, it is still possible to successfully describe all components of early postseismic deformation following the Hector Mine earthquake with afterslip at seismogenic depths [17]. It is then possible that the preferred rheologic model from Pollitz [33] was biased towards inferring a particularly low transient viscosity by neglecting to account for afterslip. This is in contrast to the present study, where we have inferred a lithospheric viscosity structure simultaneously with afterslip. While we also argue that a transient rheology is necessary to explain postseismic deformation, our preferred transient viscosity of 10^{18} Pa s is an order of magnitude larger than the transient viscosity found by [33]. Since we found that A Zener model is able to describe the available postseismic deformation following the El Mayor-Cucapah earthquake, any Burgers rheology with a steady state viscosity that is effectively infinite over five years, would also be able to describe postseismic deformation. Such a Burgers model would then be consistent with the steady state viscosities necessary for lake loading, interseismic deformation, and mantle dynamics.

Acknowledgements

We are grateful to Andy Freed for an illuminating discussion on the material in this manuscript.

This material is based on EarthScope Plate Boundary Observatory data services provided by UNAVCO through the GAGE Facility with support from the National Science Foundation (NSF) and National Aeronautics and Space Administration (NASA) under NSF Cooperative Agreement No. EAR-1261833.

This research was funded by X

[1] Aagaard, B., Williams, C., Knepley, M., Kientz, S., and Strand, L. (2009). PyLith.

[2] Argus, D. F., Heflin, M. B., Peltzer, G., Crampé, F., and Webb, F. H. (2005). Interseismic strain accumulation and anthropogenic motion in metropolitan Los Angeles. *Journal of Geophysical Research B: Solid Earth*, 110(4):1–26.

[3] Bawden, G. W., Thatcher, W., Stein, R. S., Hudnut, K. W., and Peltzer, G. (2001). Tectonic contraction across Los Angeles after removal of groundwater pumping effects. *Nature*, 412(August):812–815.

[4] Çakir, Z., Ergintav, S., Özener, H., Dogan, U., Akoglu, A. M., Meghraoui, M., and Reilinger, R. (2012). Onset of aseismic creep on major strike-slip faults. *Geology*, 40(12):1115–1118.

[5] Cetin, E., Cakir, Z., Meghraoui, M., Ergintav, S., and Akoglu, A. M. (2014). Extent and distribution of aseismic slip on the Ismetpasa segment of the North Anatolian Fault (Turkey) from Persistent Scatterer InSAR. *Geochemistry, Geophysics, Geosystems*, 15.

[6] Chopra, P. N. (1997). High-temperature transient creep in olivine rocks. *Tectonophysics*, 279:93–111.

[7] Davis, J. L., Wernicke, B. P., and Tamisiea, M. E. (2012). On seasonal signals in geodetic time series. *Journal of Geophysical Research: Solid Earth*, 117(1):1–10.

[8] Fletcher, J. M., Teran, O. J., Rockwell, T. K., Oskin, M. E., Hudnut, K. W., Mueller, K. J., Spelz, R. M., Akciz, S. O., Masana, E., Faneros, G., Fielding, E. J., Leprince, S., Morelan, A. E., Stock, J., Lynch, D. K., Elliott, A. J., Gold, P., Liu-Zeng, J., González-Ortega, A., Hinojosa-Corona, A., and González-García, J. (2014). Assembly of a large earthquake from a complex fault system: Surface rupture kinematics of the 4 April 2010 El Mayor-Cucapah (Mexico) Mw 7.2 earthquake. *Geosphere*, 10(4):797–827.

[9] Freed, A. M., Bürgmann, R., Calais, E., Freymueller, J., and Hreinsdóttir, S. (2006). Implications of deformation following the 2002 Denali, Alaska, earthquake for postseismic relaxation processes and lithospheric rheology. *Journal of Geophysical Research: Solid Earth*, 111:1–23.

[10] Freed, A. M., Bürgmann, R., and Herring, T. (2007). Far-reaching transient motions after Mojave earthquakes require broad mantle flow beneath a strong crust. *Geophysical Research Letters*, 34:1–5.

[11] Gonzalez-Ortega, A., Fialko, Y., Sandwell, D., Nava-pichardo, F. A., Fletcher, J., Gonzalez-garcia, J., Lipovsky, B., Floyd, M., and Funning, G. (2014). El Mayor-Cucapah (Mw7.2) earthquake: early near-field postseismic deformation from InSar and GPS observations. *Journal of Geophysical Research*, 119:1482–1497.

[12] Hauksson, E., Stock, J., Hutton, K., Yang, W., Vidal-Villegas, J. A., and Kanamori, H. (2011). The 2010 Mw 7.2 El mayor-cucapah earthquake sequence, Baja California, Mexico and Southernmost California, USA: Active seismotectonics along the Mexican pacific margin. *Pure and Applied Geophysics*, 168(3918):1255–1277.

[13] Hearn, E. H., McClusky, S., Ergintav, S., and Reilinger, R. E. (2009). Izmit earthquake postseismic deformation and dynamics of the North Anatolian Fault Zone. *Journal of Geophysical Research: Solid Earth*, 114(August 2008):1–21.

[14] Hetland, E. A. (2003). Postseismic relaxation across the Central Nevada Seismic Belt. *Journal of Geophysical Research*, 108(Figure 2):1–13.

[15] Hines, T. T. and Hetland, E. A. (2013). Bias in estimates of lithosphere viscosity from interseismic deformation. *Geophysical Research Letters*, 40(16):4260–4265.

[16] Hines, T. T. and Hetland, E. A. (2015). Rapid and simultaneous estimation of fault slip and heterogeneous lithospheric viscosity from post-seismic deformation. *Geophysical Journal International*, 204(1):569–582.

[17] Jacobs, A., Sandwell, D., Fialko, Y., and Sichoix, L. (2002). The 1999 (Mw7.1) Hector Mine, California, Earthquake: Near-Field Postseismic Deformation from ERS Interferometry. *Bulletin of the Seismological Society of America*, 92(May):1433–1442.

[18] Johnson, K. M., Bürgmann, R., and Freymueller, J. T. (2009). Coupled afterslip and viscoelastic flow following the 2002 Denali Fault, Alaska earthquake. *Geophysical Journal International*, 176(3):670–682.

[19] Johnson, K. M., Hilley, G. E., and Bürgmann, R. (2007). Influence of lithosphere viscosity structure on estimates of fault slip rate in the Mojave region of the San Andreas fault system. *Journal of Geophysical Research: Solid Earth*, 112:1–15.

[20] Johnson, K. M. and Segall, P. (2004). Viscoelastic earthquake cycle models with deep stress-driven creep along the San Andreas fault system. *Journal of Geophysical Research B: Solid Earth*, 109:1–19.

[21] Jónsson, S., Segall, P., Pedersen, R., and Bjornsson, G. (2003). Post-earthquake ground movements correlated to pore-pressure transients. *Nature*, 424(July):179–183.

[22] Kroll, K. A., Cochran, E. S., Richards-Dinger, K. B., and Sumy, D. F. (2013). Aftershocks of the 2010 Mw 7.2 El Mayor-Cucapah earthquake reveal complex faulting in the Yuha Desert, California. *Journal of Geophysical Research: Solid Earth*, 118(October):6146–6164.

[23] Lekic, V., French, S. W., and Fischer, K. M. (2011). Lithospheric Thinning Beneath Rifted Regions of Southern California. *Science*, 334(November):783–787.

[24] Liu, H.-P., Anderson, D. L., and Kanamori, H. (1976). Velocity dispersion due to anelasticity; implications for seismology and mantle composition. *Geophysical Journal International*, 47(1):41–58.

[25] Lundgren, P., Hetland, E. A., Liu, Z., and Fielding, E. J. (2009). Southern San Andreas-San Jacinto fault system slip rates estimated from earthquake cycle models constrained by GPS and interferometric synthetic aperture radar observations. *Journal of Geophysical Research: Solid Earth*, 114(2):1–18.

[26] Luttrell, K., Sandwell, D., Smith-Konter, B., Bills, B., and Bock, Y. (2007). Modulation of the earthquake cycle at the southern San Andreas fault by lake loading. *Journal of Geophysical Research: Solid Earth*, 112(8):1–15.

[27] McGuire, J. J. and Segall, P. (2003). Imaging of aseismic fault slip transients recorded by dense geodetic networks. *Geophysical Journal International*, 155(3):778–788.

[28] Meade, B. J. and Hager, B. H. (2005). Block models of crustal motion in southern California constrained by GPS measurements. *Journal of Geophysical Research B: Solid Earth*, 110:1–19.

[29] Murray, J. R. and Segall, P. (2005). Spatiotemporal evolution of a transient slip event on the San Andreas fault near Parkfield, California. *Journal of Geophysical Research : Solid Earth*, 110(9):1–12.

[30] Nur, A. and Mavko, G. (1974). Postseismic viscoelastic rebound. *Science*, 183(4121):204–206.

[31] Oskin, M. E., Arrowsmith, J. R., Hinojosa Corona, A., Elliott, A. J., Fletcher, J. M., Fielding, E. J., Gold, P. O., Gonzalez Garcia, J. J., Hudnut, K. W., Liu-Zeng, J., and Teran, O. J. (2012). Near-field deformation from the El Mayor-Cucapah earthquake revealed by differential LIDAR. *Science*, 335(6069):702–705.

[32] Pollitz, F., Wicks, C., and Thatcher, W. (2001). Mantle Flow Beneath a Continental Strike-Slip Fault : Postseismic Deformation After the 1999 Hector Mine Earthquake. *Science*, 1814(2001):1814–1818.

[33] Pollitz, F. F. (2003). Transient rheology of the uppermost mantle beneath the Mojave Desert,

California. *Earth and Planetary Science Letters*, 215:89–104.

[34] Pollitz, F. F., Bürgmann, R., and Thatcher, W. (2012). Illumination of rheological mantle heterogeneity by the M7.2 2010 El Mayor-Cucapah earthquake. *Geochemistry, Geophysics, Geosystems*, 13(6):1–17.

[35] Pollitz, F. F., Peltzer, G., and Bürgmann, R. (2000). Mobility of continental mantle: Evidence from postseismic geodetic observations following the 1992 Landers earthquake. *Journal of Geophysical Research*, 105(1999):8035.

[36] Rauch, H. E., Tung, F., and Striebel, C. T. (1965). Maximum likelihood estimates of linear dynamic systems. *AIAA Journal*, 3(8):1445–1450.

[37] Riva, R. E. M. and Govers, R. (2009). Relating viscosities from postseismic relaxation to a realistic viscosity structure for the lithosphere. *Geophysical Journal International*, 176:614–624.

[38] Rollins, C., Barbot, S., and Avouac, J.-P. (2015). Postseismic Deformation Following the 2010 M7.2 El Mayor-Cucapah Earthquake : Observations , Kinematic Inversions , and Dynamic Models. *Pure and Applied Geophysics*.

[39] Savage, J. C. (1990). Equivalent strike-slip earthquake cycles in half-space and lithosphere-asthenosphere earth models. *Journal of Geophysical Research*, 95:4873.

[40] Savage, J. C. and Svarc, J. L. (2009). Postseismic relaxation following the 1992 M 7.3 Landers and 1999 M 7.1 Hector Mine earthquakes , southern California. *Journal of Geophysical Research*, 114(B01401).

[41] Savage, J. C., Svarc, J. L., and Yu, S. B. (2005). Postseismic relaxation and transient creep. *Journal of Geophysical Research: Solid Earth*, 110:1–14.

[42] Segall, P. and Mathews, M. (1997). Time dependent inversion of geodetic data. *Journal of Geophysical Research*, 102.

[43] Spinler, J. C., Bennett, R. A., Walls, C., Shawn, L., and Garcia, J. J. G. (2015). Assessing long-term postseismic deformation following the M7.2 4 April 2010, El Mayor-Cucapah earthquake with implications for lithospheric rheology in the Salton Trough. *Journal of Geophysical Research: Solid Earth*, 120:3664–3679.

[44] Wei, M., Liu, Y., Kaneko, Y., Mcguire, J. J., and Bilham, R. (2015). Dynamic triggering of creep events in the Salton Trough, Southern California by regional M5.4 earthquakes constrained by geodetic observations and numerical simulations. *Earth and Planetary Science Letters*, 427:1–10.

[45] Wei, M., Sandwell, D., Fialko, Y., and Bilham, R. (2011a). Slip on faults in the Imperial Valley triggered by the 4 April 2010 Mw 7.2 El Mayor-Cucapah earthquake revealed by InSAR. *Geophysical Research Letters*, 38(January):1–6.

[46] Wei, S., Fielding, E., Leprince, S., Sladen, A., Avouac, J.-P., Helmberger, D., Hauksson, E., Chu, R., Simons, M., Hudnut, K., Herring, T., and Briggs, R. (2011b). Superficial simplicity of the 2010 El MayorCucapah earthquake of Baja California in Mexico. *Nature Geoscience*, 4(9):615–618.

[47] Yuen, D. A. and Peltier, W. R. (1982). Normal modes of the viscoelastic earth. *Geophysical Journal of the Royal Astronomical Society*, 69:495–526.

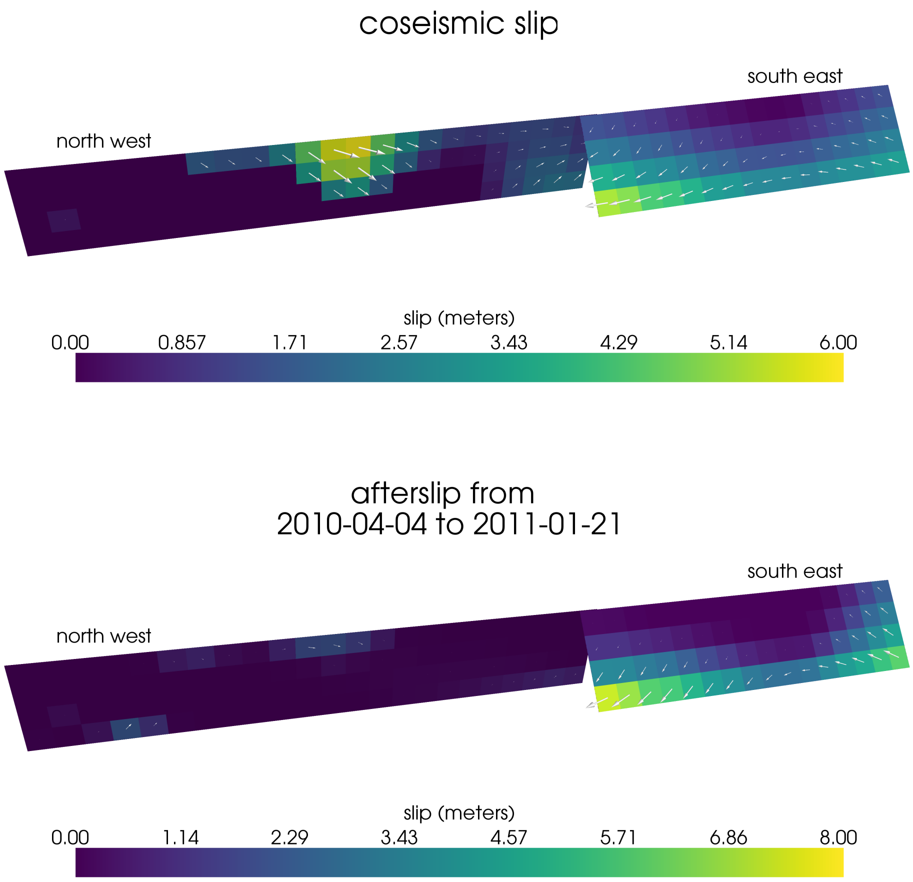
coseismic slip
south east
north west
slip (meters)
0.00
0.857
1.71
2.57
3.43
4.29
5.14
6.00
afterslip from
2010-04-04 to 2011-01-21
south east
north west
slip (meters)
0.00
1.14
2.29
3.43
4.57
5.71
6.86
8.00

Figure 11:

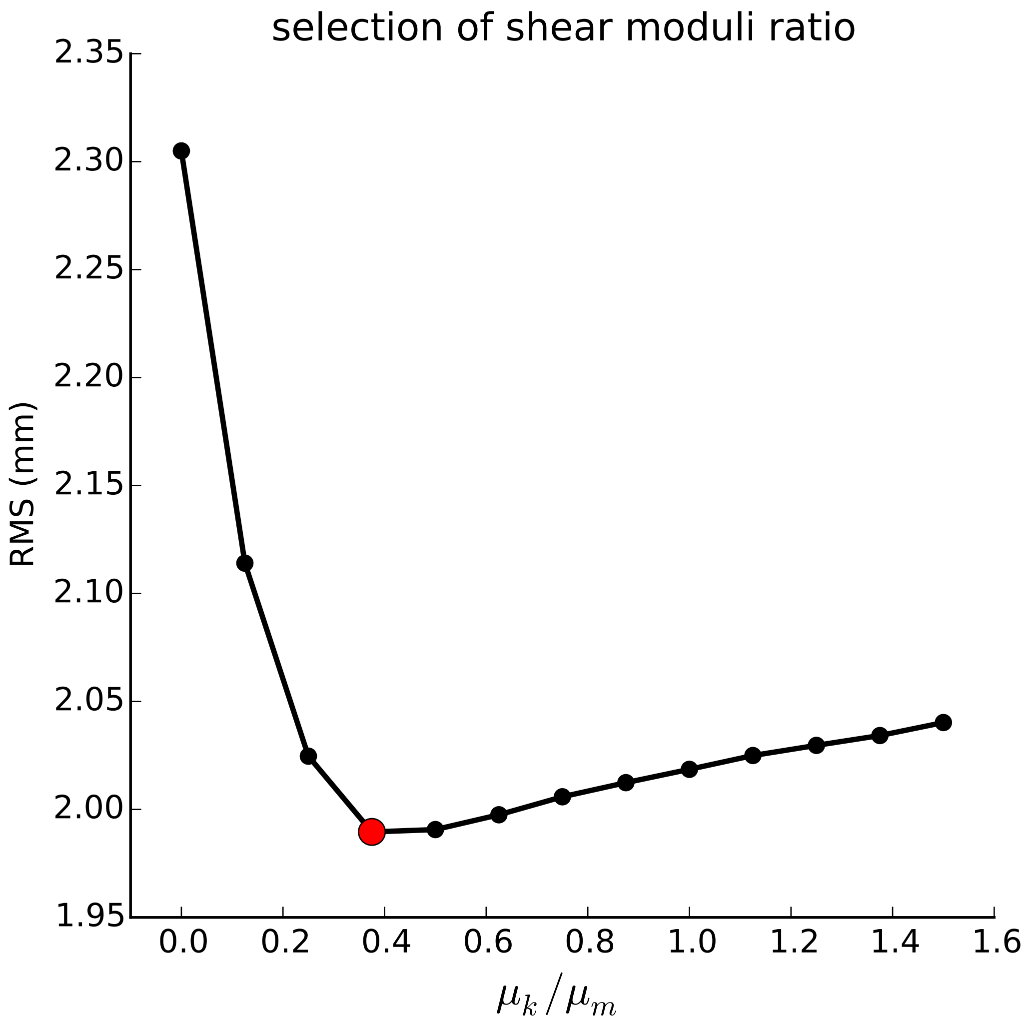

Figure 12: misfit with different shear modulus ratios

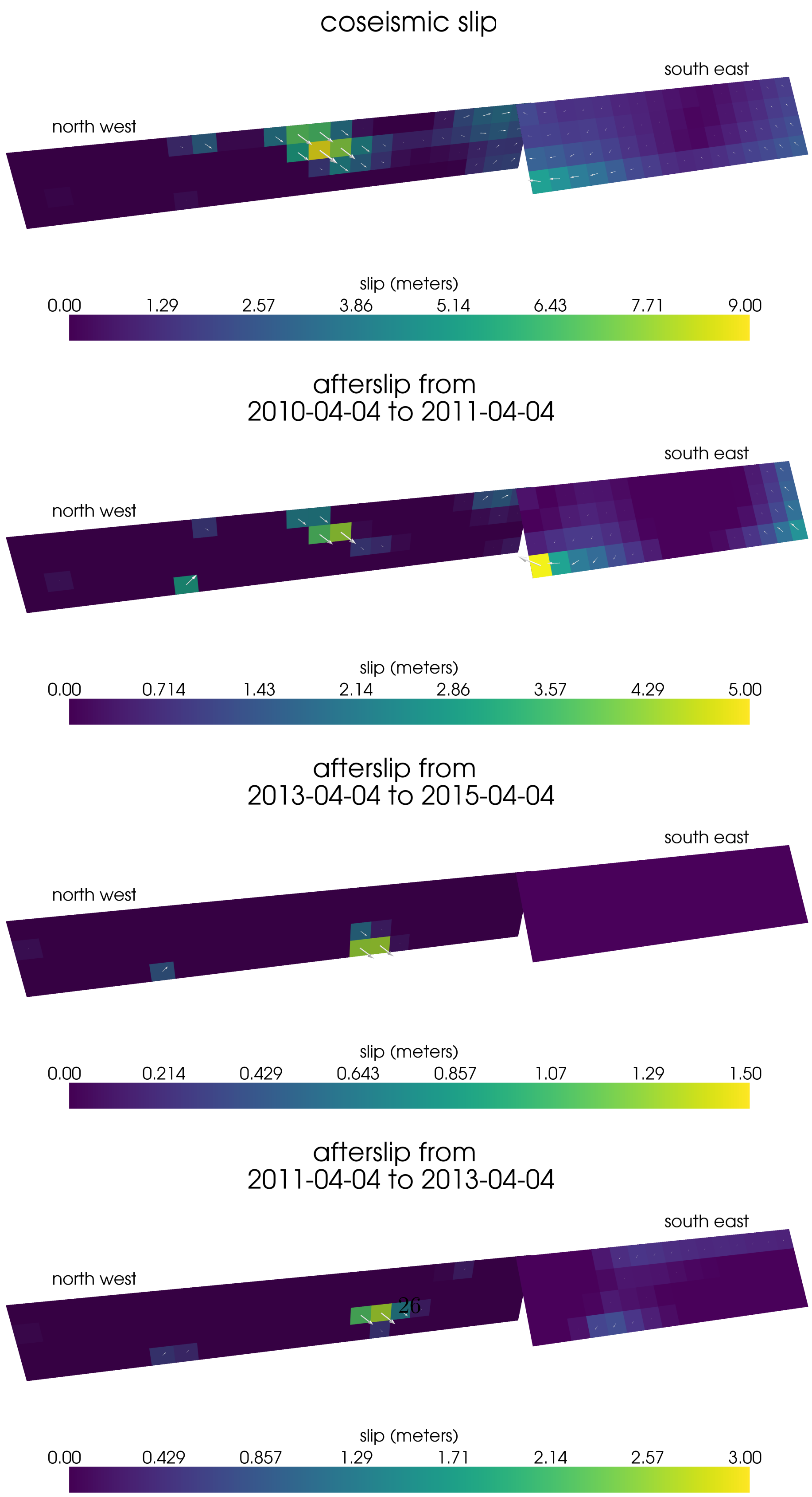
coseismic slip
north west
south east
slip (meters)
0.00 1.29 2.57 3.86 5.14 6.43 7.71 9.00
afterslip from
2010-04-04 to 2011-04-04
north west
south east
slip (meters)
0.00 0.714 1.43 2.14 2.86 3.57 4.29 5.00
afterslip from
2013-04-04 to 2015-04-04
north west
south east
slip (meters)
0.00 0.214 0.429 0.643 0.857 1.07 1.29 1.50
afterslip from
2011-04-04 to 2013-04-04
north west
south east
slip (meters)
0.00 0.429 0.857 1.29 1.71 2.14 2.57 3.00

Figure 13:

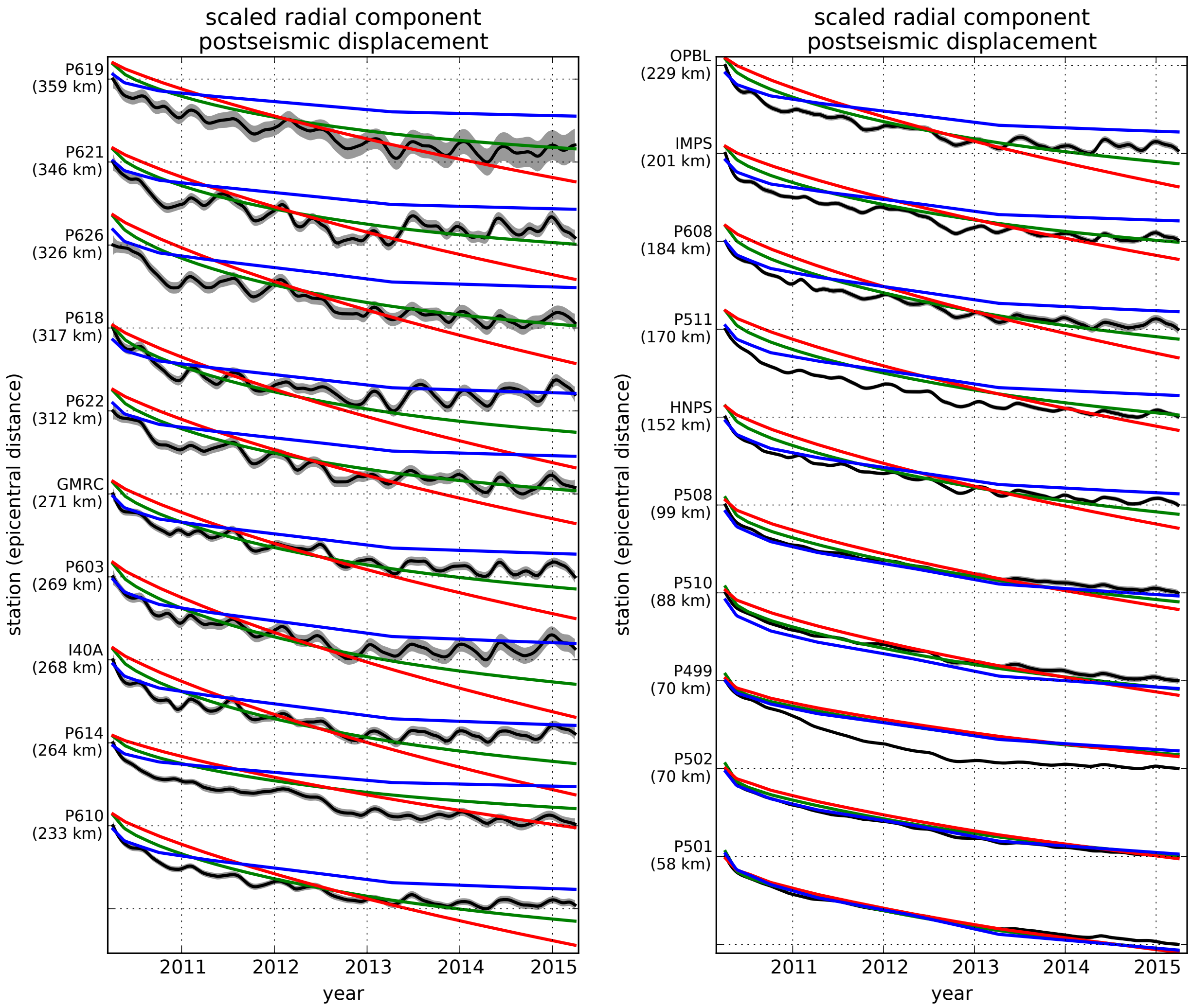
scaled radial component
postseismic displacement
P619
(359 km)
P621
(346 km)
P626
(326 km)
P618
(317 km)
P622
(312 km)
GMRC
(271 km)
P603
(269 km)
I40A
(268 km)
P614
(264 km)
P610
(233 km)
station (epicentral distance)
2011
2012
2013
2014
2015
year
scaled radial component
postseismic displacement
OPBL
(229 km)
IMPS
(201 km)
P608
(184 km)
P511
(170 km)
HNPS
(152 km)
P508
(99 km)
P510
(88 km)
P499
(70 km)
P502
(70 km)
P501
(58 km)
station (epicentral distance)
2011
2012
2013
2014
2015
year

Figure 14: